# A Novel Sharpening Approach for Superresolving Multiresolution Optical Images

Claudia Paris, *Member, IEEE*, José Bioucas-Dias, *Fellow, IEEE*, and Lorenzo Bruzzone, *Fellow, IEEE*

***Abstract*— This paper aims to provide a compact superresolution formulation specific for multispectral (MS) multiresolution optical data, i.e., images characterized by different scales across different spectral bands. The proposed method, named multiresolution sharpening approach (MuSA), relies on the solution of an optimization problem tailored to the properties of those images. The superresolution problem is formulated as the minimization of an objective function containing a data-fitting term that models the blurs and downsamplings of the different bands and a patch-based regularizer that promotes image self-similarity guided by the geometric details provided by the high-resolution bands. By exploiting the approximately low-rank property of the MS data, the ill-posedness of the inverse problem in hand is strongly reduced, thus sharply improving its conditioning. The state-of-the-art color block-matching and 3D filtering (C-BM3D) image denoiser is used as a patch-based regularizer by leveraging the "plug-and-play" framework: the denoiser is plugged into the iterations of the alternating direction method of multipliers. The main novelties of the proposed method are: 1) the introduction of an observation model tailored to the specific properties of (MS) multiresolution images and 2) the exploitation of the high-spatial-resolution bands to guide the grouping step in the color block-matching and 3D filtering (C-BM3D) denoiser, which constitutes a form of regularization learned from the high-resolution channels. The results obtained on the real and synthetic Sentinel 2 data sets give an evidence of the effectiveness of the proposed approach.**

***Index Terms*— Alternating direction method of multipliers (ADMM), color block-matching and 3D filtering (C-BM3D), dimensionality reduction, multispectral (MS) multiresolution images, plug-and-play, remote sensing, self-similarity, superresolution.**

## I. Introduction

SATELLITE remote sensing images have been extensively employed in many large-scale applications, such as land-use/cover classification, environmental monitoring, and change detection. Although the multispectral (MS) sensors provide worldwide coverage with a fast revisit time, the physical limits of the radiometric resolution of the detectors impose tradeoffs to the achievable spatial–spectral resolutions. To have a reasonable signal-to-noise ratio (SNR), the spatial resolution must be lower when the higher spectral resolution is required. In contrast, high spatial resolution can be obtained at the cost of losing spectral resolution. For these reasons, in the last years, many sensors have been designed to acquire low-spatial-resolution MS bands together with a single high-spatial-resolution band (panchromatic image), taken in a large spectral interval. The panchromatic image provides the high-resolution geometric details while guaranteeing a spectral range that spans most of the spectra of the MS bands.

By fusing the MS bands and the panchromatic image, it is possible to generate spatially enhanced MS data, which provides a better understanding of the observed scene. To this end, a number of fusion methods have been introduced in the literature, namely, those collectively called pansharpening algorithms [1], [2] formulated under different frameworks, such as component substitution (CS), multiresolution analysis (MRA), model-based variational regularization, and Bayesian inference.

CS methods aim to detect a transformation that separates the spatial and the spectral information of the original data into different components. In the projected space, the spatial component can be substituted with the panchromatic image, thus leading to an enhanced MS product. To reduce the distortion introduced by the fusion step, it is necessary to identify a projected space where the panchromatic image and the replaced component are strongly correlated. Among the different projection methods employed, the principal component analysis (PCA) [3], [4], the intensity–hue–saturation transform technique [5]–[7], and the Gram–Schmidt transformation [8], [9] have been widely used. In spite of the large amount CS-based pansharpening works developed and published in the last decade, this research direction is sill attracting the attention of the research community [10]–[12].

MRA is another class of pansharpening methods. Here, the spatial details are extracted through a multiresolution decomposition of the panchromatic image and injected into the interpolated MS bands. MRA methods do a better job in preserving the spectral characteristics of the MS data than CS ones, since no transformation is involved. Several modalities have been introduced to extract the spatial details, such as the discrete wavelet transform [13]–[16] or other kinds of pyramidal representations [1], [17], [18]. High-pass filtering (HPF) fusion methods [19], [20] inject the high-frequency details into the resampled MS data. The geometric details are typically obtained by taking the difference between the panchromatic image and its blurred version.

Manuscript received March 8, 2018; revised June 5, 2018; accepted August 1, 2018. Date of publication September 26, 2018; date of current version February 25, 2019. This work was supported by the Portuguese Fundação para a Ciência e Tecnologia under Grant UID/EEA/50008/2013 and Grant ERANETMED/0001/2014. *(Corresponding author: Claudia Paris.)*

C. Paris and L. Bruzzone are with the Department of Information Engineering and Computer Science, University of Trento, 38123 Trento, Italy (e-mail: claudia.paris@unitn.it; lorenzo.bruzzone@ing.unitn.it).

J. Bioucas-Dias is with the Instituto de Telecomunicações, Instituto Superior Técnico, Universidade de Lisboa, 1049-001 Lisbon, Portugal (e-mail: bioucas@lx.it.pt).

Color versions of one or more of the figures in this paper are available online at http://ieeexplore.ieee.org.

Digital Object Identifier 10.1109/TGRS.2018.2867284

Bayesian and variational regularization methods are *model-based* [21]; they rely on an *observation model* that accounts for blur, dowsampling, and noise, and on *regularization* (prior information in Bayesian terms) that mitigates the usual ill-posedness of the pansharpening inverse problems. The high-resolution image is usually obtained by solving an optimization problem that superresolves all the spectral bands simultaneously. Studies in [22] and [23] are two paradigmatic examples of this line of attack: the former is based on spectral and spatial sparsity inducing priors and the latter on total variation regularization.

Although pansharpening algorithms successfully deal with the fusion of MS images acquired together with a panchromatic band, a growing number of sensors are started to acquire MS multiresolution images having more than one high-spatial-resolution channel [e.g., Moderate Resolution Imaging Spectroradiometer (MODIS), Sentinel-2 (S2), and Advanced Spaceborne Thermal Emission and Reflection Radiometer (ASTER)]. Typically, the high-spatial-resolution bands cover the visible range, while the narrow-spectral-resolution bands are provided at lower spatial resolution. In the literature, only a few papers have addressed the superresolution of MS multiresolution images. Most of them focus on the superresolution of specific spectral channels of the MS multiresolution data by using pansharpening approaches [24]–[26]. Aiazzi *et al.* [24] sharpen the ASTER thermal infrared (TIR) bands by injecting the geometric information present in the visible or near-infrared (VNIR) channels using the generalized Laplacian pyramid algorithm. To achieve the same goal, Fasbender *et al.* [25] propose a general Bayesian data fusion approach that exploits the 15-m VNIR bands to sharpen the 90-m TIR bands of the ASTER data. Similarly, Sirguey *et al.* [26] employ a wavelet-based MRA to fuse the spatial resolution of 250-m MODIS bands into the 500-m MODIS bands for snow mapping in mountainous environments. The work in [27] presents a superresolution method that enhances the 500-m MODIS bands by taking advantage from the correlation between the spectral channels. The method defines a nonlinear regression model that uses the 250-m MODIS channels and the NDVI as predictors. Moreover, a normalization step is applied to increase the spatial resolution of the 500 m bands while preserving the radiometric consistency of the superresolved channels. The regression modeling is also exploited in [28] and [29], where the 250-m MODIS high-spatial-resolution bands are fused into the 500-m bands by considering geostatistical approaches based on kriging.

Several methods adapt pansharpening algorithms to the multiresolution case [30]–[32]. Tonooka [30] proposes a method to increase the spatial resolution of the short-wave infrared (SWIR) and TIR of ASTER images at the 15-m resolution of the VNIR bands. The main idea is to exploit the spectral similarity to superresolve the spectral bands. The use of the spectral similarity for superresolving MS multiresolution images was conceptualized by Selva *et al.* [33], where they defined a new paradigm for hypersharpening. Two schemes were proposed to extend the pansharpening algorithms to the case of MS images having multiple high-resolution bands, namely, the "synthesized band scheme" and the "selected band scheme." The "selected band scheme" selects for each coarse resolution band the high resolution one having the largest correlation, while the "synthesized band scheme" synthesizes a panchromatic image from the high-resolution band set. In [31], the "synthesized band scheme" is employed to enhance the 20-m S2 bands by using the 10-m S2 bands considering the area-to-point regression Kriging (ATPRK) pansharpening method. For each coarse band, the panchromatic image is determined adaptively as a linear combination of the four high-spatial-resolution bands. In [32], 21 different pansharpening algorithms have been compared to increase the spatial resolution of the 20-m bands of S2 by selecting a suitable 10-m band as a panchromatic image. Lanaras *et al.* [34] formulate a convex inverse problem tailored to the superresolution of S2 data. The discontinuities, learned from the high-resolution bands, are encoded into a regularizer used to sharpen the 20- and 60-m bands. Brodu [35] presents a method to superresolve MS multiresolution data and tests it on the real S2 images. Assuming that the proportion of objects within a pixel area is the same for all the bands, the high-resolution channels are used to separate band-independent information. The obtained geometric information is then employed to unmix the low-resolution pixels while preserving their overall reflectance. Although this is one of the few superresolution works which enhance all the lower spatial channels of S2, the results obtained are not competitive with the state of the art.

Recent studies started to use denoisers to superresolve natural images [36] or for image restoration [37]. In this context, one of the most employed denoisers is BM3D, namely, block matching and 3-D filtering, which is particularly effective due to its capability of promoting nonlocal patch self-similarity properties of the images based on sparse representations [36]. This denoiser stacks together similar 2-D image patches in 3-D arrays (groups), the so-called *grouping* step, to perform nonlocal image modeling, thus leading to effective noise attenuation. The recently presented color version of the BM3D [38] extends the denoising algorithm to the case of color images corrupted by additive white Gaussian noise. First, the RGB image is converted into the luminance-chrominance color space (YCbCr). Then, the *grouping* step is applied only to the luminance band, which typically shows a higher SNR with respect to the chrominances. Finally, the color image is denoised by imposing a grouping constraint on both chrominances, i.e., reusing the same grouping obtained on the luminance. Egiazarian and Katkovnik [39] use the C-BM3D to superresolve natural images. The study demonstrates the importance of having high-resolution data to accurately estimate groups of similar patches to obtain accurate superresolution results. In the framework of superresolving MS multiresolution images, the use of these denoisers as regularizers can be extremely useful to promote nonlocal image self-similarity while exploiting the geometric details provided by the high-resolution channels to detect the groups of similar patches.

### A. Contribution

This paper is built around the superresolution of a single MS multiresolution image, with the aim of employing

the geometric details present in the high-resolution bands to sharpen the low-resolution ones. The proposed approach: 1) defines a quadratic fitting term that accounts for the blur and downsampling degradation mechanisms; 2) takes advantage from the low-rank nature of the MS image to formulate the problem in the latent space defined by the representation coefficients; 3) adopts the "plug-and-play" framework to plug the C-BM3D denoiser [38] into the iterations of an alternating direction method of multipliers (ADMM) algorithm, in order to exploit the self-similarity property of the MS images; and 4) learns a patch-based spatial prior from the high-spatial-resolution channels to sharpen the lower spatial resolution bands. The optimization is performed by using the split augmented Lagrangian shrinkage algorithm (SALSA) solver [40], [41], which is an efficient and flexible instance of ADMM tailored to multiple convex terms.

In the literature, the sharpening of MS multiresolution images has been addressed by adapting pansharperning techniques to infer a spatially enhanced MS product. In practice, however, the pansharpening paradigm requires: 1) only one high-spatial-resolution channel and 2) the spectral overlap between the high-spatial-resolution bands and the low resolution ones. In this paper, we relax those constrains by providing a compact formulation tailored to the specific properties of the MS multiresolution images. Different from recent works that use denoisers to superresolve natural images (i.e., images characterized by three bands, RGB, having the same spatial resolution), the proposed method exploits the geometric detail provided by the high-resolution channels to guide the *grouping* step of the C-BM3D to detect similar patches within the image. This strongly improves the robustness of the method and the quality of the results with respect to the standard use of a denoiser, which operates on the noisy low-resolution data.

To assess the effectiveness of the proposed method, experiments have been carried out on real and simulated MS multiresolution S2 images containing bands at 10, 20, and 60 m. Results have been evaluated qualitative and quantitatively by investigating the spectral distortions on the synthetic data set.

### B. Outline

The remained of this paper is organized as follows. Section II describes the notation and the problem formulation used in this paper. Section III presents the proposed superresolution method in terms of the observation model, dimensionality reduction, and regularization and the algorithm to solve it. Section IV describes the considered data set, while Section V illustrates and discusses the experimental results. Finally, Section VI draws the conclusions.

## II. Notation and Problem Formulation

MS images are usually represented as 3-D arrays. However, when the bands have different sizes, this representation is no more adequate. In this paper, the spectral bands are represented as column vectors where the pixels are arranged in the lexicographic order. The bands are then concatenated to represent the observed data. Let us define the columnwise concatenation of $I$ column vectors $\mathbf{a}_i \in \mathbb{R}^{m_i}$, for $i = 1, \ldots, I$, as $(\mathbf{a}_1; \mathbf{a}_2; \ldots; \mathbf{a}_I) := [\mathbf{a}_1^{\mathrm{T}}; \mathbf{a}_2^{\mathrm{T}}; \ldots; \mathbf{a}_I^{\mathrm{T}}]^{\mathrm{T}} \in \mathbb{R}^{m_1+m_2+\cdots+m_I}$. When all vectors have the same size, $(\mathbf{a}_1; \ldots; \mathbf{a}_I)$ is the so-called vec operator acting on the columns of the matrix $\mathbf{A} = [\mathbf{a}_1, \mathbf{a}_2, \ldots, \mathbf{a}_I]$.

Let us assume to have an image characterized by $L_b$ spectral bands having $d_k$, for $k = 1, \ldots, K$, ground sampling distances (GSDs), such that $L_b = L_1 + L_2 + \cdots + L_K$, and $L_k$ denotes the number of bands with the same GSD $d_k$. Of course, the resolution of the spectral bands decreases as the GSD increases. Without loss of generality, we assume that $d_1 = 1$.

Let $\mathbf{y}_j$ be the column vector representing the $j$th observed spectral band, with $j = 1, \ldots, L_b$. The observed image is represented as $\mathbf{y} = (\mathbf{y}_1; \mathbf{y}_2; \ldots; \mathbf{y}_{L_b}) \in \mathbb{R}^{n_o}$, where $n_o = n \cdot (L_1 + L_2/d_2^2 + \cdots + L_K/d_K^2)$ and $n$ is the number of pixels of the bands with the highest resolution.

The enhanced MS image $\mathbf{x} = (\mathbf{x}_1, \mathbf{x}_2, \ldots, \mathbf{x}_{L_b}) \in \mathbb{R}^{n_u}$ is the vertical concatenation of the $L_b$ spectral bands having size $n$ (i.e., all bands at the highest spatial resolution) with a number of unknowns $n_u = n \cdot L_b$. Since the target image $\mathbf{x}$ has the same spatial resolution for all the bands, it can also be represented as a 2-D matrix, where each line corresponds to a spectral band, containing the lexicographically ordered pixels of that band, i.e., $\mathbf{X} = [\mathbf{x}_1; \mathbf{x}_2; \ldots; \mathbf{x}_{L_b}]^T \in \mathbb{R}^{L_b \times n}$, with $\mathbf{x} = \mathrm{vec}(\mathbf{X}^{\mathrm{T}})$.

## III. Superresolution Method

Fig. 1 shows the flowchart of the proposed method, which embodies four main steps: 1) the formulation of an observation model tailored to the specific properties of the MS multiresolution image; 2) a dimensionality reduction step performed to reduce the number of unknowns; 3) the use of the C-BM3D denoiser as a regularizer based on the geometric details provided by the high-resolution bands; and 4) the optimization performed using the SALSA solver to deal with nonsmooth convex regularization terms with low computational burden.

### A. Observation Model

Assuming linear operation of the imaging sensor, the observed model may be written as

$$\mathbf{y} = \mathbf{MBx} + \mathbf{n} \tag{1}$$

where $\mathbf{B} = \mathrm{bkdiag}(\mathbf{B}_1, \ldots, \mathbf{B}_{L_b}) \in \mathbb{R}^{L_b n \times L_b n}$ is a block-circulant–circulant-block matrix whose block diagonal elements $\mathrm{bkdiag}(\cdot_1, \ldots, \cdot_{L_b})$ represent the 2-D spatial blurring matrices modeling the point spread functions (PSFs) of the different spectral channels with respect to the highest spatial resolution. Note that because each subblock acts separately on each spectral channel, we can accurately model the PSFs that affect the different bands according to the specific properties of the considered sensor. The blur is assumed to be a cyclic convolution. Although the assumption of having periodic boundary is not realistic, it does not lead to significant artifacts in the superresolved image while strongly reducing the computational effort [42].

The block diagonal matrix $\mathbf{M} = \mathrm{bkdiag}(\mathbf{M}_1, \ldots, \mathbf{M}_{L_b}) \in \mathbb{R}^{L_b n \times L_b n}$ represents subsampling, where the blocks are applied to $\mathbf{x}$ in order to obtain $\mathbf{y}$. While for the high-resolution

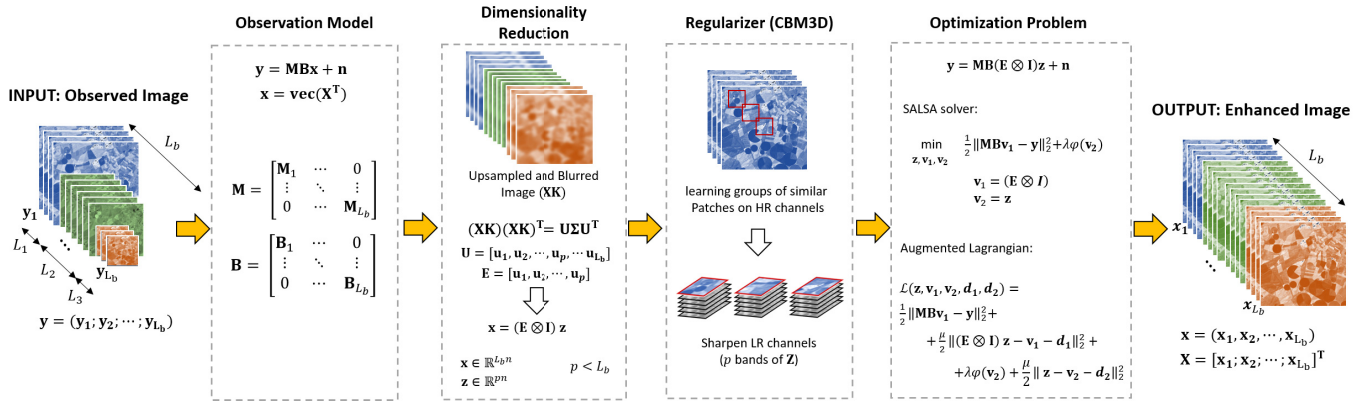


Fig. 1. Flowchart of the proposed approach for superresolving MS multiresolution images (MuSA).

bands, the blocks are identity matrices $\mathbf{I}$, for the other channels, they are subsets of the rows of the identity matrix, accounting for the uniform subsampling of each individual band. Finally, $\mathbf{n}$ denotes the zero-mean Gaussian additive noise. For the sake of simplicity, the noise is assumed to be identically and independently distributed (i.i.d.) across bands and pixels.

### B. Dimensionality Reduction

The considered superresolution problem is extremely ill-posed, since the number of unknowns is much greater than the number of observations (i.e., $n_u \gg n_o$). To cope with this issue, we took advantage from the fact that MS images live in a subspace of low dimensionality: due to the strong correlation between the spectral bands, the original data $\mathbf{X}$ have low-rank, namely, the spectral vectors associated with the image pixels live, with a very good approximation, in a low-dimensional subspace. Thus, the matrix $\mathbf{X}$ can be accurately approximated by the linear combinations of a small number of basis vectors, i.e.,

$$\mathbf{X} = \mathbf{EZ} \tag{2}$$

where the columns of matrix $\mathbf{E} \in \mathbb{R}^{L_b \times p}$, with $p < L_b$, holds the subspace basis vectors and $\mathbf{Z} \in \mathbb{R}^{p \times n}$ holds the representation coefficients. Noting that $\mathbf{x} = \text{vec}(\mathbf{X}^{\mathrm{T}})$, and by using the properties of the vec operator, we may write

$$\begin{aligned} \mathbf{x} &= \text{vec}((\mathbf{EZ})^{\mathrm{T}}) = \text{vec}(\mathbf{IZ}^{\mathrm{T}}\mathbf{E}^{\mathrm{T}}) \\ &= (\mathbf{E} \otimes \mathbf{I})\text{vec}(\mathbf{Z}^{\mathrm{T}}) = (\mathbf{E} \otimes \mathbf{I})\mathbf{z} \end{aligned} \tag{3}$$

where $\mathbf{z} = \text{vec}(\mathbf{Z}^{\mathrm{T}}) \in \mathbb{R}^{pn}$ are the representation coefficients of $\mathbf{x}$ with respect to $\mathbf{E}$.

However, $\mathbf{X}$ is the image that we aim to estimate, while the observed data $\mathbf{y}$ are the blurred and subsampled version of it. Although we do not have $\mathbf{X}$, we can estimate the subspace by considering its smoothed version $\mathbf{XK}$, where $\mathbf{K}$ is a matrix acting on all bands and representing the strongest convolution of the considered MS multiresolution data. Even though $\mathbf{XK}$ provides less information with respect to the original image, due to a large number of pixels and spectral variability of the corresponding spectra, it is very likely that span($\mathbf{X}$)= span($\mathbf{XK}$), i.e., the subspaces spanned by the columns $\mathbf{X}$ and of $\mathbf{XK}$ are equal.

To generate an approximation of $\mathbf{XK}$, first, we upsample all the low-resolution observed MS spectral channels (i.e., the observed channels $\mathbf{y}_i$, such that $d_i > 1$ for $i = 1, \ldots, L_b$) to the highest resolution of the considered MS data by means of cubic interpolation. Then, for each spectral channel, we tailor the amount of blur to apply in order to have the same blur (the strongest of the considered MS data) for all the bands.

To learn span($\mathbf{XK}$), we compute the eigendecomposition span($(\mathbf{XK})(\mathbf{KX})^{\mathrm{T}}$), of size $L_b \times L_b$, which is very light, since the matrix is very small. Let

$$(\mathbf{XK})(\mathbf{KX})^{\mathrm{T}} = \mathbf{U}\Sigma\mathbf{U}^{\mathrm{T}} \tag{4}$$

be the eigendecomposition of $(\mathbf{XK})(\mathbf{KX})^{\mathrm{T}}$, where the columns of $\mathbf{U}$ hold the eigenvectors and the diagonal of $\Sigma$ holds the corresponding eigenvalues, which are nonnegative and ordered by nonincreasing values. We set $\mathbf{E} = [\mathbf{u}_1, \ldots, \mathbf{u}_p]$, where $\mathbf{u}_i$, for $i = 1, \ldots, L_b$, is the $i$th column of $\mathbf{U}$. The value of $p$ is set such that more than 99% of the image energy is preserved.

### C. Regularization

The low-rank representation (2) allows us to formulate the superresolution imaging inverse problem in hand with respect to the coefficients $\mathbf{Z}$ instead of $\mathbf{X}$, thus reducing the number of unknowns from $L_b n$ to $pn$ (keep in mind that $p < L_b$). From a conditioning point of view, computing $\mathbf{Z}$ should then be easier than computing $\mathbf{X}$. In particular, if the number of unknowns is now lower than the number of observed variables, i.e., if $pn < n \cdot (L_1 + L_2/d_2^2 + \cdots + L_K/d_K^2)$, the inverse problem is no longer ill-posed. However, owing to the low-pass PSFs and noise, the estimation of $\mathbf{Z}$ is still ill-conditioned, thus calling for regularization.

In order to select a suitable regularizer for $\mathbf{Z}$, we point out that: 1) the bands of $\mathbf{X}$, as images from the real world, are self-similar and 2) the structure of self-similarity is the same across all bands of $\mathbf{X}$, as the bands are reflectances (or radiances) from the same surface. Since the bands of $\mathbf{Z}$, herein termed *eigenimages*, are linear combinations of the bands of $\mathbf{X}$,

they are also self-similar having the structure of self-similarity of $\mathbf{X}$.

In our approach, we selected the C-BM3D denoiser [38], as it is one of the fastest state-of-the-art patch-based denoisers for color images, promotes self-similar solutions, and allows to build the self-similarity structure from an external image, and in spite of being conceived for color images, it may be easily adapted to our $p$ eigenimages.

### D. Optimization Problem

Let us suppose for a while that we have a regularizer $\varphi$ that promotes the self-similar eigenimages. Based on the observation model (1) and $\varphi$, the estimation of $\mathbf{Z}$ is formulated as the optimization

$$\min_{\mathbf{z}} \frac{1}{2}\|\mathbf{MB}(\mathbf{E}\otimes\mathbf{I})\mathbf{z}-\mathbf{y}\|_2^2+\lambda\varphi(\mathbf{z}) \tag{5}$$

where the quadratic term is the data misfit, which promotes solutions compatible with the observed data, and $\lambda \geq 0$ is the regularization parameter that tunes the relative weight between the two terms.

To solve the optimization (5), we use the SALSA [41], which is an instance of ADMM. Following the SALSA steps, we rewrote the original optimization (5) in the equivalent form:

$$\begin{aligned}\min_{\mathbf{z},\mathbf{v}_1,\mathbf{v}_2}\ & \frac{1}{2}\|\mathbf{MB}\mathbf{v}_1-\mathbf{y}\|_2^2+\lambda\varphi(\mathbf{v}_2)\\ \text{s.t:}\ \ & \mathbf{v}_1=(\mathbf{E}\otimes\mathbf{I})\mathbf{z}\\ & \mathbf{v}_2=\mathbf{z}.\end{aligned} \tag{6}$$

The augmented Lagrangian for (6) is

$$\begin{aligned}&\mathcal{L}(\mathbf{z},\mathbf{v}_1,\mathbf{v}_2,\mathbf{d}_1,\mathbf{d}_2)\\ &\quad=\frac{1}{2}\|\mathbf{MB}\mathbf{v}_1-\mathbf{y}\|_2^2+\frac{\mu}{2}\|(\mathbf{E}\otimes\mathbf{I})\mathbf{z}-\mathbf{v}_1-\mathbf{d}_1\|_2^2\\ &\qquad+\lambda\varphi(\mathbf{v}_2)+\frac{\mu}{2}\|\mathbf{z}-\mathbf{v}_2-\mathbf{d}_2\|_2^2\end{aligned} \tag{7}$$

where $\mathbf{d}_1$ and $\mathbf{d}_2$ are the scaled Lagrange multipliers for $\mathbf{v}_1$ and $\mathbf{v}_2$ and $\mu > 0$ is a penalty parameter. SALSA is an iterative procedure that, in each iteration, implements sequentially the following steps:

$$\mathbf{z} := \arg\min_{\mathbf{z}} \mathcal{L}(\mathbf{z},\mathbf{v}_1,\mathbf{v}_2,\mathbf{d}_1,\mathbf{d}_2) \tag{8}$$

$$\mathbf{v}_1 := \arg\min_{\mathbf{v}_1} \mathcal{L}(\mathbf{z},\mathbf{v}_1,\mathbf{v}_2,\mathbf{d}_1,\mathbf{d}_2) \tag{9}$$

$$\mathbf{v}_2 := \arg\min_{\mathbf{v}_2} \mathcal{L}(\mathbf{z},\mathbf{v}_1,\mathbf{v}_2,\mathbf{d}_1,\mathbf{d}_2) \tag{10}$$

$$\mathbf{d}_1 := \mathbf{d}_1-((\mathbf{E}\otimes\mathbf{I})\mathbf{z}-\mathbf{v}_1) \tag{11}$$

$$\mathbf{d}_2 := \mathbf{d}_2-(\mathbf{z}-\mathbf{v}_2). \tag{12}$$

Minimization (8), with respect to $\mathbf{z}$, is quadratic and, having into consideration that $\mathbf{E}^{\mathrm{T}}\mathbf{E}=\mathbf{I}$, its solution is

$$\mathbf{z}=(\mathbf{E}\otimes\mathbf{I})(\mathbf{v}_1+\mathbf{d}_1+\mathbf{v}_2+\mathbf{d}_2)/2. \tag{13}$$

Minimization (9), with respect to $\mathbf{v}_1$, is also quadratic and has the solution

$$\mathbf{v}_1=(\mathbf{B}^{\mathrm{T}}\mathbf{M}^{\mathrm{T}}\mathbf{MB}+\mu\mathbf{I})^{-1}(\mathbf{B}^{\mathrm{T}}\mathbf{M}^{\mathrm{T}}\mathbf{y}+\mu(\mathbf{E}\otimes\mathbf{I})\mathbf{z}-\mu\mathbf{d}_1). \tag{14}$$

Given that $\mathbf{B}$ represents the cyclic convolutions and $\mathbf{M}$ represents the uniform subsampling, $\mathbf{v}_1$ may be computed efficiently in the frequency domain [43].

Minimization (10), with respect to $\mathbf{v}_2$, is

$$\mathbf{v}_2 := \arg\min_{\mathbf{v}_2} \lambda\varphi(\mathbf{v}_2)+\frac{\mu}{2}\|\mathbf{z}-\mathbf{v}_2-\mathbf{d}_2|_2^2 \tag{15}$$

whose solution is the so-called proximity operator [44] of $\varphi\lambda/\mu$, denoted as $\mathrm{prox}_{\varphi\lambda/\mu}$, computed at $(\mathbf{z}-\mathbf{d}_2)$. We may then write

$$\mathbf{v}_2 := \mathrm{prox}_{\varphi\lambda/\mu}(\mathbf{z}-\mathbf{d}_2).$$

At this point, we adopt the "plug-and-play" scheme [45], which consists in replacing $\mathrm{prox}_{\varphi\lambda/\mu}$ with a state-of-the-art denoiser, the C-BM3D in our approach. C-BM3D version [38] accepts the variance of the additive noise and a reference image to compute the patch similarity and therefore computing the groups of similar patches. By noting that (15) may be interpretable as a pure denoising problem where the noise is i.i.d. with standard deviation $\sigma=\sqrt{\lambda/\mu}$, we set

$$\mathbf{v}_2 := \mathrm{CBM3D}(\mathbf{z}-\mathbf{d}_2,\overline{\mathbf{y}}_h,\sigma)$$

where $\overline{\mathbf{y}}_h$ denotes a linear combination of the four fine bands. A regression model built between the $p$th coarse band and the four high-resolution bands is applied to estimate the weights to generate $\overline{\mathbf{y}}$.

SALSA, as an ADMM instance, is guaranteed to converge, provided that the terms of the objective function are convex and the null space of linear operator between $\mathbf{z}$ and $(\mathbf{v}_1,\mathbf{v}_2)$ contains only the zero vector [41]. The second condition is satisfied in our setup due to the constraint $\mathbf{v}_2=\mathbf{z}$. However, the first condition cannot be directly assessed, since we do not have $\varphi$. In the plug-and-play framework, a sufficient condition for convergence is that the denoiser plugged into the ADMM iterations is the proximity operator of some convex function. This is true if and only if the denoiser is nonexpansive and a subgradient of some convex function (see [46]). This is not the case for most state-of-the-art denoisers (see [47] for an exception), which has fostered active research in this topic.

Fortunately, the convergence of our plug-and-play instance is guaranteed, since the denoiser is a proximity operator. This is the case of C-BM3D when the grouping step is fixed, as it is our case. Details about the properties of BM3D using fixed grouping are provided in [36]. The pseudocode for the proposed algorithm, called multiresolution sharpening approach (MuSA), is shown in Algorithm 1.

## IV. Data Sets and Design of the Experiments

In this section, we present the real and simulated data sets used for the experimental tests. The procedure to generate the simulated data set is described in detail. Then, we present the experimental setup in terms of implementation parameters and quality indexes used to evaluate the effectiveness of the proposed method.

TABLE I
SPECTRAL PROPERTIES OF THE S2 DATA

| | B1 | B2 | B3 | B4 | B5 | B6 | B7 | B8 | B8a | B9 | B10 | B11 | B12 |
|---|---|---|---|---|---|---|---|---|---|---|---|---|---|
| **Central wavelength (nm)** | 443 | 490 | 560 | 665 | 705 | 740 | 783 | 842 | 865 | 945 | 1380 | 1610 | 2190 |
| **Spectral Width (nm)** | 20 | 65 | 35 | 30 | 15 | 15 | 20 | 115 | 20 | 20 | 30 | 90 | 180 |
| **Spatial Resolution (m)** | 60m | 10m | 10m | 10m | 20m | 20m | 20m | 10m | 20m | 60m | 60m | 20m | 20m |

**Algorithm 1:** MuSA

**Input**: $\mathbf{y}$ - observed image
$\mathbf{B}$ - blur matrix
$\mathbf{M}$ - decimation matrix
$\mathbf{E}$ - estimated subspace matrix
$\mu$ - penalty parameter
$\lambda$ - regularization parameter
$N$ - number of iterations

**Init**: $\mathbf{v}_1^{(0)} = 0,\ \mathbf{v}_2^{(0)} = 0,\ \mathbf{d}_1^{(0)} = 0,\ \mathbf{d}_2^{(0)} = 0$

**for** $k = 0 : N$ **do**

$$\mathbf{z}^{k+1} := (\mathbf{E} \otimes \mathbf{I})(\mathbf{v}_1^k + \mathbf{d}_1^k + \mathbf{v}_2^k + \mathbf{d}_2^k)/2$$
$$\mathbf{v}_1^{k+1} := (\mathbf{B}^{\mathrm{T}}\mathbf{M}^{\mathrm{T}}\mathbf{M}\mathbf{B} + \mu\mathbf{I})^{-1} (\mathbf{B}^{\mathrm{T}}\mathbf{M}^{\mathrm{T}}\mathbf{y} + \mu(\mathbf{E} \otimes \mathbf{I})\mathbf{z}^{k+1} - \mu\mathbf{d}_1^k)$$
$$\mathbf{v}_2^{k+1} := \mathrm{CBM3D}(\mathbf{z} - \mathbf{d}_2, \overline{\mathbf{y}}_h, \sqrt{\lambda/\mu})$$
$$\mathbf{d}_1^{k+1} = \mathbf{d}_1^k - ((\mathbf{E} \otimes \mathbf{I})\mathbf{z}^{k+1} - \mathbf{v}_1^{k+1})$$
$$\mathbf{d}_2^{k+1} := \mathbf{d}_2^k - (\mathbf{z}^k - \mathbf{v}_2^k)$$

**end**

**Output**: $\mathbf{x} = (\mathbf{E} \otimes \mathbf{I})\mathbf{z}$

### A. Data Set Description

The proposed method is tested on the real and simulated S2 images that have 13 spectral bands acquired at three different spatial resolutions (see Table I), i.e., $L_1 = 10$ m, $L_2 = 20$ m, and $L_3 = 60$ m. In the presented experiments, we do not consider the 60-m band containing the cirrus information (B10) that is used to perform the atmospheric correction [48].

To simulate the S2 images, we employed the hyperspectral images acquired by the NASA Airborne Visible/Infrared Imaging Spectrometer (AVIRIS) sensor, which provides 224 narrow contiguous spectral bands from 0.4 to 2.5 $\mu$m [49]. Four different AVIRIS images were considered to test the proposed approach in different environmental scenarios, thus generating: 1) the *coastal* data set; 2) the *mountainous* data set; 3) the *urban* data set; and 4) the *crop* data set. The first two data sets were acquired at a spatial resolution of 5 m, while the urban data set and the crop data set were acquired at a spatial resolution of 3.5 and 3.2 m, respectively.

First, we created the ground-truth images (i.e., the super-resolved S2 data having all bands at 10 m) which are used for quantitative evaluation according to Wald's protocol [20]. To this end, we low-pass filtered all the bands of the AVIRIS images and then subsampled the blurred images by a factor of 2 for the coastal and urban data sets and a factor of 3 for the other data sets, obtaining a spatial resolution of approximately 10 m. Gaussian low-pass filters with the support of size $15 \times 15$ and $\sigma = 1.2$ for the mountainous and coastal data sets, $\sigma = 1.5$ for the urban data set, and $\sigma = 1.6$ for the crop data set were used. The spectral properties of S2 were simulated by applying its spectral response to the AVIRIS images. Finally, we added the i.i.d. Gaussian noise with an SNR of 40 dB, where $\mathrm{SNR} = \|\mathbf{x}\|_2^2/(\sigma^2\, n\, L_b)$.

To generate the simulated multiresolution S2 data, the bands of the ground-truth images were further smoothed and subsampled. To have a realistic simulation of the S2 sensor, the PSFs of the Gaussian smoothing were set equal to the ones estimated in the data quality report provided by the European Space Agency on S2 products [50]. Subsampling factors of 2 and 6 were applied to generate the 20- and 60-m spectral bands, respectively.

Complementary to the simulated data, we tested the proposed method on the real S2 data acquired on the same geographical area of the AVIRIS data. Fig. 2 shows a true color representation of the simulated S2 images and the corresponding real S2 data for each data sets. Note that there are some changes on the ground between the simulated and the real images due to the different temporal acquisition. The AVIRIS data were acquired on August 3, 2013 for the crop data set, November 9, 2011 for the coastal and mountainous data sets, and May 10, 2006 for the urban data set. The real S2 data were acquired on March 11, 2017 (Tile T10SEH) for the crop data set and September 11, 2017 for all the other data sets (Tile T11SMS).

### B. Experimental Setup

For all the experiments, both on the real and simulated data sets, we used the same experimental setup: augmented Lagrange parameter $\mu = 0.6$, regularization parameter $\lambda = 0.005$, and SALSA iterations $N = 130$. This value of $N$ has yielded systematical negligible values of the primal and dual residuals, which is the valid stopping criteria [51].

The subspace $\mathbf{E}$ was estimated by considering the five singular vectors corresponding to the largest singular values, which ensure the preservation of more than 99% of the energy of the original images. Since the energy per band varies considerably across the spectrum, we normalize the spectral bands before applying MuSA, such that their mean squared intensities are equal to 1.

To quantitatively assess the performances of MuSA and of the competitors, we calculate the following performance indexes.

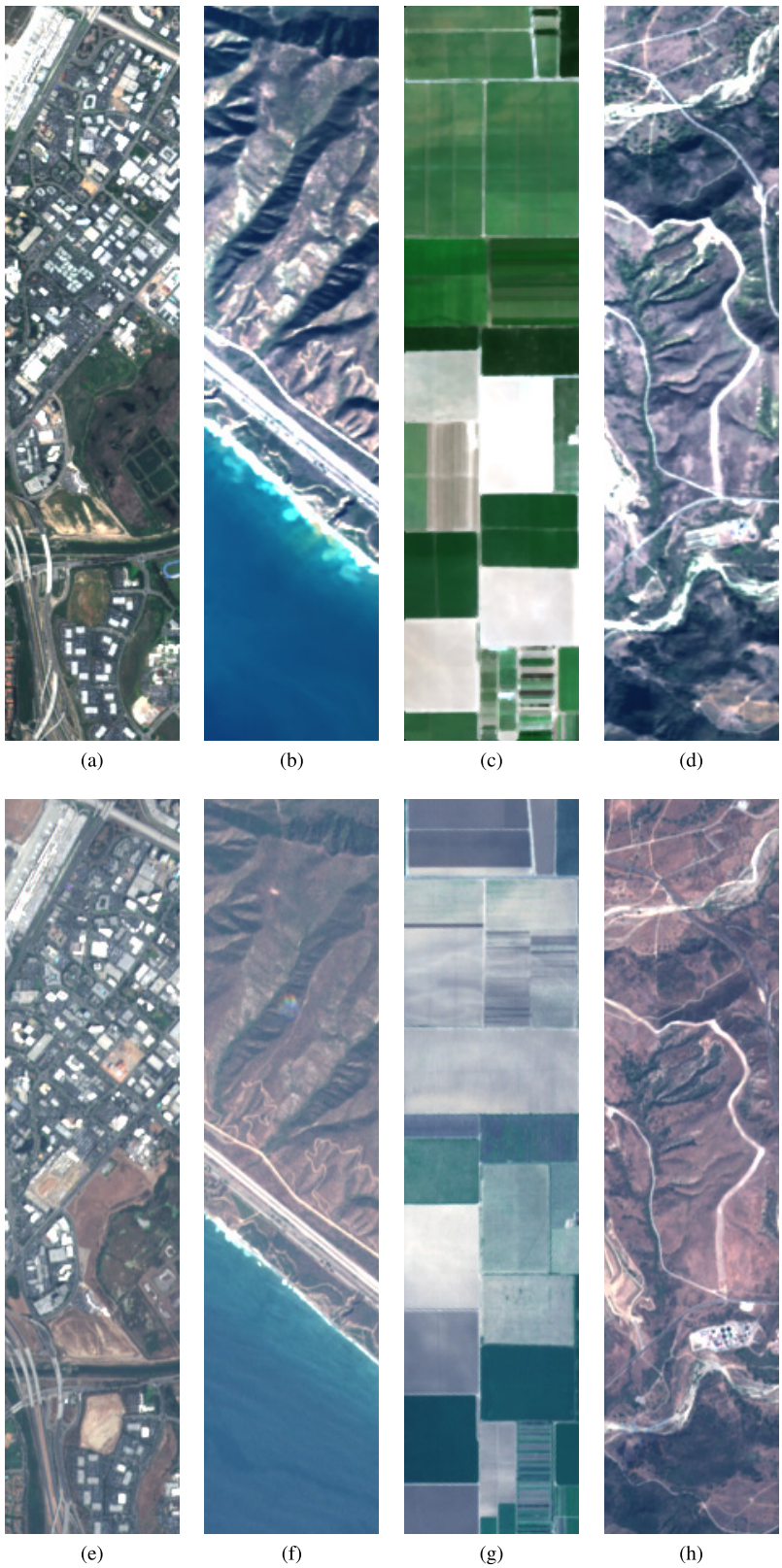


Fig. 2. Simulated S2 images and real S2 images. True color composition of the simulated S2 images for (a) urban data set, (b) coastal data set, (c) crop data set, and (d) mountainous data set. True color composition of the real S2 data for (e) urban data set, (f) coastal data set, (g) crop data set, and (h) mountainous data set.

1) *Signal-to-Reconstruction Error (SRE), in dB, per Band*:

$$\mathrm{SRE}_i = 10 \log_{10} \frac{\|\mathbf{x}_i\|^2}{\|\mathbf{x}_i - \hat{\mathbf{x}}_i\|_2^2} \tag{16}$$

where $\mathbf{x}_i$ and $\hat{\mathbf{x}}_i$ are the ground-truth spectral band $i$ and the corresponding superresolved spectral band, respectively.

2) *Spectral Angle Mapper (SAM) [52] in Degrees*:

$$\mathrm{SAM}(\mathbf{X}, \hat{\mathbf{X}}) = \frac{1}{n} \sum_i \arccos \left( \frac{\mathbf{X}_{:,i}^{\mathrm{T}} \hat{\mathbf{X}}_{:,i}}{\|\mathbf{X}_{:,i}\|_2 \|\hat{\mathbf{X}}_{:,i}\|_2} \right) \quad (17)$$

where $\mathbf{X}_{:,i}$ and $\hat{\mathbf{X}}_{:,i}$ are the spectra of the $i$th pixel for the ground-truth and the estimated S2 image, respectively.

3) *Root-Mean-Square Error (RMSE)*:

$$\mathrm{RMSE}(\mathbf{X}, \hat{\mathbf{X}}) = \frac{\|\mathbf{X} - \hat{\mathbf{X}}\|}{n}. \quad (18)$$

4) *Universal Image Quality Index (UIQI):* It is proposed in [53]

$$\mathrm{Q}(\mathbf{x}_i, \hat{\mathbf{x}}_i) = \frac{1}{W} \sum_{j=1}^{W} \frac{\sigma_{\mathbf{x}_{i,j} \hat{\mathbf{x}}_{i,j}}}{\sigma_{\mathbf{x}_{i,j}} \sigma_{\hat{\mathbf{x}}_{i,j}}} \times \frac{2\mu_{\mathbf{x}_{i,j}} \mu_{\hat{\mathbf{x}}_{i,j}}}{\mu_{\mathbf{x}_{i,j}}^2 + \mu_{\hat{\mathbf{x}}_{i,j}}^2} \times \frac{2\sigma_{\mathbf{x}_{i,j}} \sigma_{\hat{\mathbf{x}}_{i,j}}}{\sigma_{\mathbf{x}_{i,j}}^2 + \sigma_{\hat{\mathbf{x}}_{i,j}}^2}$$

where $\mathbf{x}_i$ and $\hat{\mathbf{x}}_i$ denote the ground-truth and the super-resolved band $i$,respectively, $\mathbf{x}_{i,j}$ and $\hat{\mathbf{x}}_{i,j}$ denote the values of $\mathbf{x}_i$ and $\hat{\mathbf{x}}_i$ in a sliding window of size $32 \times 32$ pixels centered at pixel $j$, respectively, $\sigma_{\mathbf{x}_{i,j} \hat{\mathbf{x}}_{i,j}}$ is the covariance between $\mathbf{x}_{i,j}$ and $\hat{\mathbf{x}}_{i,j}$, and $\sigma_{\mathbf{x}_{i,j}}$ and $\mu_{\mathbf{x}_{i,j}}$ are the standard deviation and the mean value of $\mathbf{x}_{i,j}$, while $\sigma_{\hat{\mathbf{x}}_{i,j}}$ and $\mu_{\hat{\mathbf{x}}_{i,j}}$ are the standard deviation and the mean value of $\hat{\mathbf{x}}_{i,j}$.

To extend the UIQI index to the multiband case, we simply average the band indexes obtained as follows:

$$\mathrm{Q}(\mathbf{X}, \hat{\mathbf{X}}) = \frac{1}{n} \sum_i \mathrm{Q}(\mathbf{x}_i, \hat{\mathbf{x}}_i). \quad (19)$$

## V. Experimental Results

In this section, first, we present the quantitative results obtained on the simulated data sets by comparing the proposed approach with five state-of-the-art pansharpening algorithms adapted to the multiresolution case. Then, qualitative results are presented on real S2 data for each data set.

### A. Experiments on Simulated Data Sets

To assess the effectiveness of the proposed approach, the method was compared with five different baselines. The first and the second baselines are the simple bicubic upsampling (Bicubic) and the ATPRK presented in [31], which achieved the best numerical results on the real S2 images compared with several pansharpening methods. The third baseline is the MRA pansharpening algorithm, such as HPF [1], while the last two baselines are the CS pansharpening algorithms, such as partial replacement adaptive component substitution (PRACS) [54] and PCA [19]. To apply those methods to the considered MS multiresolution data, we extracted a single panchromatic band from the four high-resolution bands available in the S2 images by considering the "selected" and the "synthesized" strategies conceptualized in [33]. While the "selected" scheme identifies the panchromatic band with the high-resolution band having the largest correlation with the considered coarse one, the "synthesized" band is determined adaptively as a linear combination of the four high-resolution bands as presented in [31].

Table II shows the quantitative results obtained by comparing the superresolved S2 images with the ground-truth images on the different simulated data sets by using: 1) Bicubic; 2) ATPRK; 3) MuSA; 4) HPF; 5) PRACS; and 6) PCA. The best results are marked in bold font. For each pansharpening algorithm, we tested both the "selected" and the "synthesized" strategies, reporting the best result per band. From the results obtained, it turned out that MuSA and ATPRK have achieved the best SRE per band, while among the standard pansharpening methods, the MRA HPF has achieved better results compared with the CS algorithms.

MuSA has outperformed all the other methods in bands B6 B7 B8a and B9 for all the data sets and achieved the best results for almost all the data sets in bands B1 and B5. The most challenging bands are B11 and B12, belonging to the SWIR range that is far away from the spectral view point from the high-resolution bands. However, the minimum SRE achieved by MuSA is 20.69 dB (for B12 in the urban data set) with an average SRE over the data sets of 25.30 and 25.56 dB for B11 and B12, respectively. Similar results are achieved by ATPRK and HPF, while PRACS and PCA are resulted in an average SRE lower than 19 dB for both the bands.

Moreover, MuSA has achieved an accurate SRE for both the 60- and 20-m bands regardless of the initial spatial resolution. Thus, for all the data sets, the method obtained an SRE on the 60-m bands that ranges from a minimum of 27.81 dB (B9 coastal data set) to a maximum of 35.36 dB (B9 crop data set). In contrast, the HPF, the PRACS, and the PCA methods have resulted in poor SRE for B9 in some data sets, i.e., HPF obtained 20.05 dB, PRACS 18.03 dB, and PCA 18.62 dB in the urban data set.

The capability of MuSA of delivering more balanced results across the bands with respect to the baselines is confirmed by the results obtained in terms of average SRE, SAM, RMSE, and UIQI. Here, the proposed method has achieved the best results for almost all the data sets with an average SAM, RMSE, and UIQI across the data sets of 1.07, 32.99, and 0.95, respectively. Note that achieving balanced results across the bands can be extremely important for applications where the spectral contribution of all the bands is employed, such as image classification or spectral unmixing.

### B. Experiments on Real Data Sets

Complementary to simulated data, we tested the proposed approach on the real S2 data acquired in the same geographical areas to provide qualitative results. Fig. 3–6 visually compare the results of all baselines to the one obtained with MuSA for crops, coastal, mountainous, and urban data sets, respectively. To evaluate the results obtained for both the 60- and 20-m spectral bands, a false color composite of bands B1-B9-B1, B5-B6-B7, and B8a-B11-B12 is provided together with a true color composite of the 10-m resolution bands, which shows the geometric detail present in the scene. The results obtained on the real S2 data confirm what we observed on the simulated data from the quantitative view point. The 60-m bands are accurately superresolved only by MuSA and ATRPK, whereas all the other methods provide the blurred

TABLE II

RELATIVE SRE (dB), SAM (IN DEGREE), RMSE, AND UIQI BETWEEN THE SUPERRESOLUTION IMAGE AND THE GROUND-TRUTH (SIMULATED IMAGES) PER BAND FOR: 1) BICUBIC; 2) ATPRK; 3) MuSA; 4) HPF; 5) PRACS; AND 6) PCA

| **SNR** | **40 dB** | | | | | | | | | | | |
|---|---|---|---|---|---|---|---|---|---|---|---|---|
| **Method** | **SRE** | | | | | | | | | **SAM** | **RMSE** | **UIQI** |
| | **B1** | **B5** | **B6** | **B7** | **B8a** | **B9** | **B11** | **B12** | **Average** | | | |
| **Crop Dataset** | | | | | | | | | | | | |
| **Bicubic** | 18.25 | 32.64 | 29.76 | 28.97 | 28.46 | 22.61 | 28.33 | 24.56 | 26.70 | 1.54 | 142.35 | 0.89 |
| **ATPRK** | 30.16 | 32.13 | 32.90 | 32.91 | 32.91 | 31.70 | 30.31 | 29.39 | 31.55 | 1.24 | 72.27 | 0.93 |
| **MuSA** | **33.67** | 34.37 | **36.79** | **38.15** | **40.15** | **35.36** | 29.80 | 29.33 | **34.70** | **0.80** | **53.33** | **0.98** |
| **HPF** | 26.35 | **36.29** | 35.84 | 35.58 | 34.58 | 29.75 | **32.68** | **29.89** | 32.62 | 0.95 | 67.71 | 0.96 |
| **PRACS** | 28.46 | 25.60 | 34.91 | 34.75 | 37.24 | 30.80 | 20.61 | 19.75 | 29.01 | 1.94 | 129.15 | 0.93 |
| **PCA** | 26.41 | 24.31 | 33.96 | 33.64 | 35.94 | 29.68 | 19.03 | 18.43 | 27.68 | 2.32 | 151.68 | 0.91 |
| **Coastal Dataset** | | | | | | | | | | | | |
| **Bicubic** | 25.68 | 24.03 | 22.93 | 22.71 | 21.85 | 15.56 | 20.86 | 19.41 | 21.63 | 2.29 | 52.27 | 0.75 |
| **ATPRK** | 32.28 | 30.49 | 31.85 | 32.40 | 31.08 | 25.67 | **24.45** | 23.72 | 28.99 | 1.85 | 20.55 | 0.77 |
| **MuSA** | 32.40 | **30.63** | **31.96** | **34.79** | **36.08** | **27.81** | 24.07 | **24.15** | **30.23** | **1.13** | **18.35** | **0.85** |
| **HPF** | **32.96** | 28.16 | 31.51 | 31.99 | 30.12 | 21.44 | 20.91 | 19.38 | 27.06 | 1.76 | 26.12 | 0.78 |
| **PRACS** | 31.36 | 17.84 | 27.02 | 31.80 | 35.41 | 24.53 | 13.82 | 12.75 | 24.32 | 3.19 | 47.42 | 0.76 |
| **PCA** | 32.53 | 16.32 | 26.52 | 30.40 | 32.48 | 22.46 | 12.09 | 10.46 | 22.91 | 4.37 | 56.70 | 0.73 |
| **Mountainous Dataset** | | | | | | | | | | | | |
| **Bicubic** | 22.92 | 23.67 | 22.66 | 22.41 | 21.81 | 16.85 | 21.28 | 20.50 | 21.51 | 2.40 | 61.74 | 0.87 |
| **ATPRK** | 31.67 | 30.86 | 30.91 | 31.31 | 31.77 | 28.00 | 23.16 | 24.39 | 29.01 | 1.79 | 25.39 | 0.98 |
| **MuSA** | **34.08** | **32.84** | **33.69** | **34.90** | **35.68** | **32.30** | **26.15** | **28.07** | **32.21** | **1.08** | **17.91** | **0.99** |
| **HPF** | 29.86 | 30.11 | 31.33 | 31.27 | 29.53 | 23.58 | 24.58 | 25.26 | 28.19 | 1.52 | 27.58 | 0.98 |
| **PRACS** | 30.62 | 31.92 | 30.02 | 30.31 | 30.03 | 22.57 | 19.08 | 20.35 | 26.86 | 2.03 | 34.20 | 0.97 |
| **PCA** | 29.24 | 29.81 | 28.41 | 28.57 | 28.15 | 21.88 | 17.29 | 18.58 | 25.24 | 2.46 | 41.19 | 0.96 |
| **Urban Dataset** | | | | | | | | | | | | |
| **Bicubic** | 17.29 | 20.71 | 19.89 | 19.15 | 18.11 | 14.31 | 18.18 | 16.33 | 18.00 | 3.44 | 177.67 | 0.79 |
| **ATPRK** | 30.83 | 30.15 | 31.38 | 31.67 | 30.76 | 27.90 | **23.73** | **22.36** | 28.60 | 1.60 | 46.73 | **0.99** |
| **MuSA** | **31.32** | **30.91** | **32.51** | **35.42** | **35.79** | **30.27** | 21.18 | 20.69 | **29.76** | **1.27** | **42.38** | 0.98 |
| **HPF** | 24.00 | 29.73 | 28.07 | 27.59 | 25.45 | 20.05 | 22.54 | 20.64 | 24.76 | 1.76 | 76.02 | 0.96 |
| **PRACS** | 23.07 | 28.62 | 27.24 | 26.83 | 25.38 | 18.03 | 19.66 | 17.75 | 23.32 | 2.01 | 85.38 | 0.94 |
| **PCA** | 23.06 | 26.46 | 25.39 | 25.08 | 23.91 | 18.62 | 16.65 | 15.28 | 21.81 | 2.32 | 100.10 | 0.92 |
| **Average Results across all Datasets** | | | | | | | | | | | | |
| **Bicubic** | 21.03 | 25.26 | 23.81 | 23.31 | 22.56 | 17.33 | 22.16 | 20.20 | 21.96 | 2.42 | 108.51 | 0.83 |
| **ATPRK** | 31.24 | 30.91 | 31.76 | 32.07 | 31.63 | 28.32 | **25.41** | 24.97 | 29.54 | 1.62 | 41.24 | 0.92 |
| **MuSA** | **32.87** | **32.19** | **33.74** | **35.81** | **36.92** | **31.44** | 25.30 | **25.56** | **31.73** | **1.07** | **32.99** | **0.95** |
| **HPF** | 28.29 | 31.07 | 31.69 | 31.61 | 29.92 | 23.71 | 25.18 | 23.79 | 28.16 | 1.50 | 49.36 | 0.92 |
| **PRACS** | 28.38 | 26.00 | 29.80 | 30.92 | 32.01 | 23.98 | 18.29 | 17.65 | 25.88 | 2.30 | 74.04 | 0.90 |
| **PCA** | 27.81 | 24.23 | 28.57 | 29.42 | 30.12 | 23.16 | 16.27 | 15.68 | 24.41 | 2.87 | 87.42 | 0.88 |
| **Ideal Values** | - | - | - | - | - | - | - | - | - | 0 | 0 | 1 |

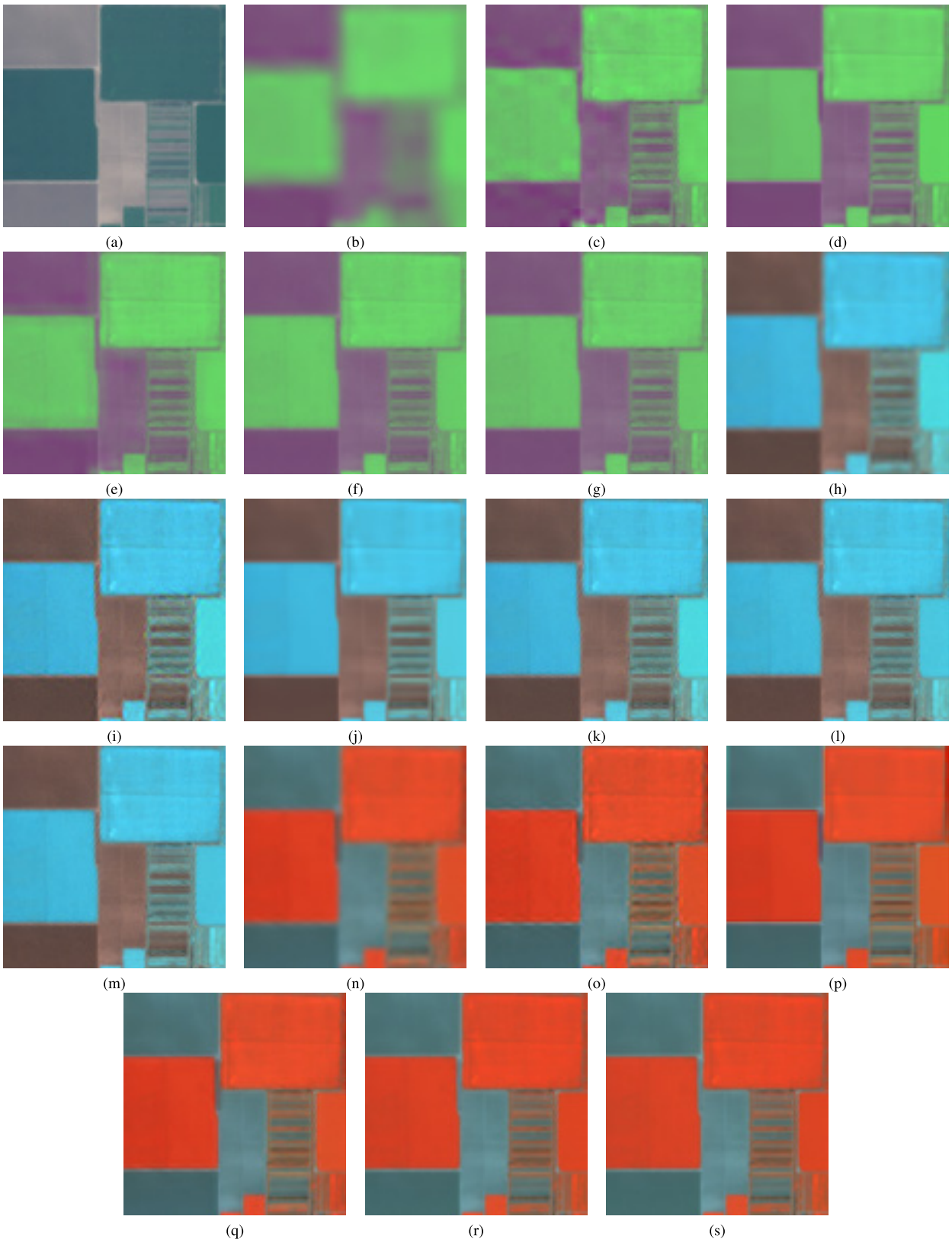


Fig. 3. Qualitative results on the real S2 images for the crop data set. (a) True color composite that represents the geometric detail of the scene. (b)–(g) False color composite of bands 1 and 9 (60 m). (h)–(m) False color composite of bands 5–7 (20 m). (n)–(s) False color composite of bands 8a, 11, and 12 (20 m).

results for all data sets (see Figs. 3–6). This is clearly visible in the urban data sets (see Fig. 6) characterized by many high-frequency details, which are properly recovered by MuSA while smoothing the other pansharpening algorithms. From the false color composites of bands B8a-B11-B12, the low SRE results achieved by PRACS and PCA on the simulated data

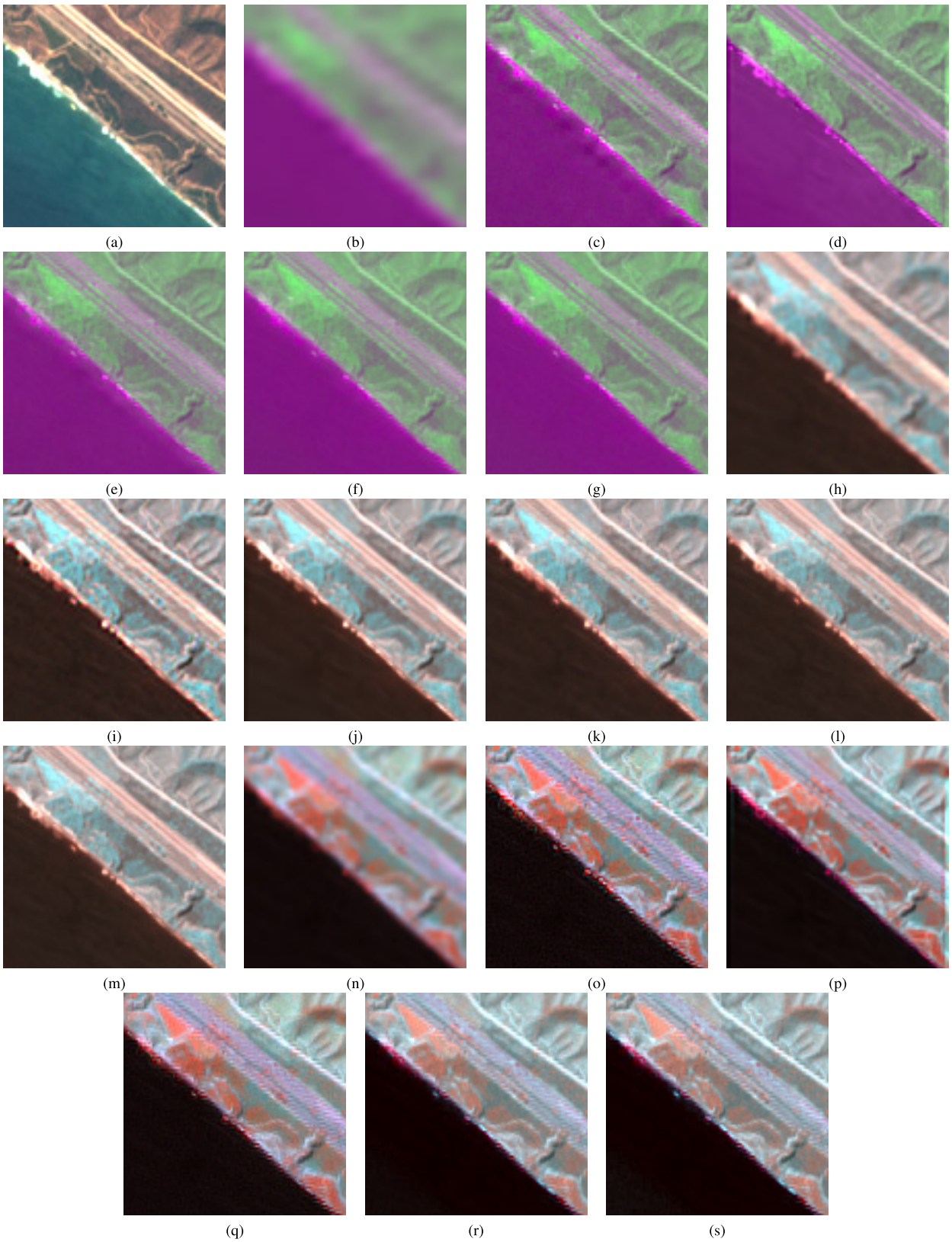


Fig. 4. Qualitative results on the real S2 images for the coastal data set. (a) True color composite that represents the geometric detail of the scene. (b)–(g) False color composite of bands 1 and 9 (60 m). (h)–(m) False color composite of bands 5–7 (20 m). (n)–(s) False color composite of bands 8a, 11, and 12 (20 m).

sets are confirmed in the real data sets, since the superresolved images present many artifacts. The presence of artifacts is also visible in the images obtained with ATPRK and HPF for the coastal and the urban data sets (see Figs. 4 and 6). In contrast, MuSA reproduces accurate spatial textures while preserving the spectral properties of the low-resolution S2 bands.

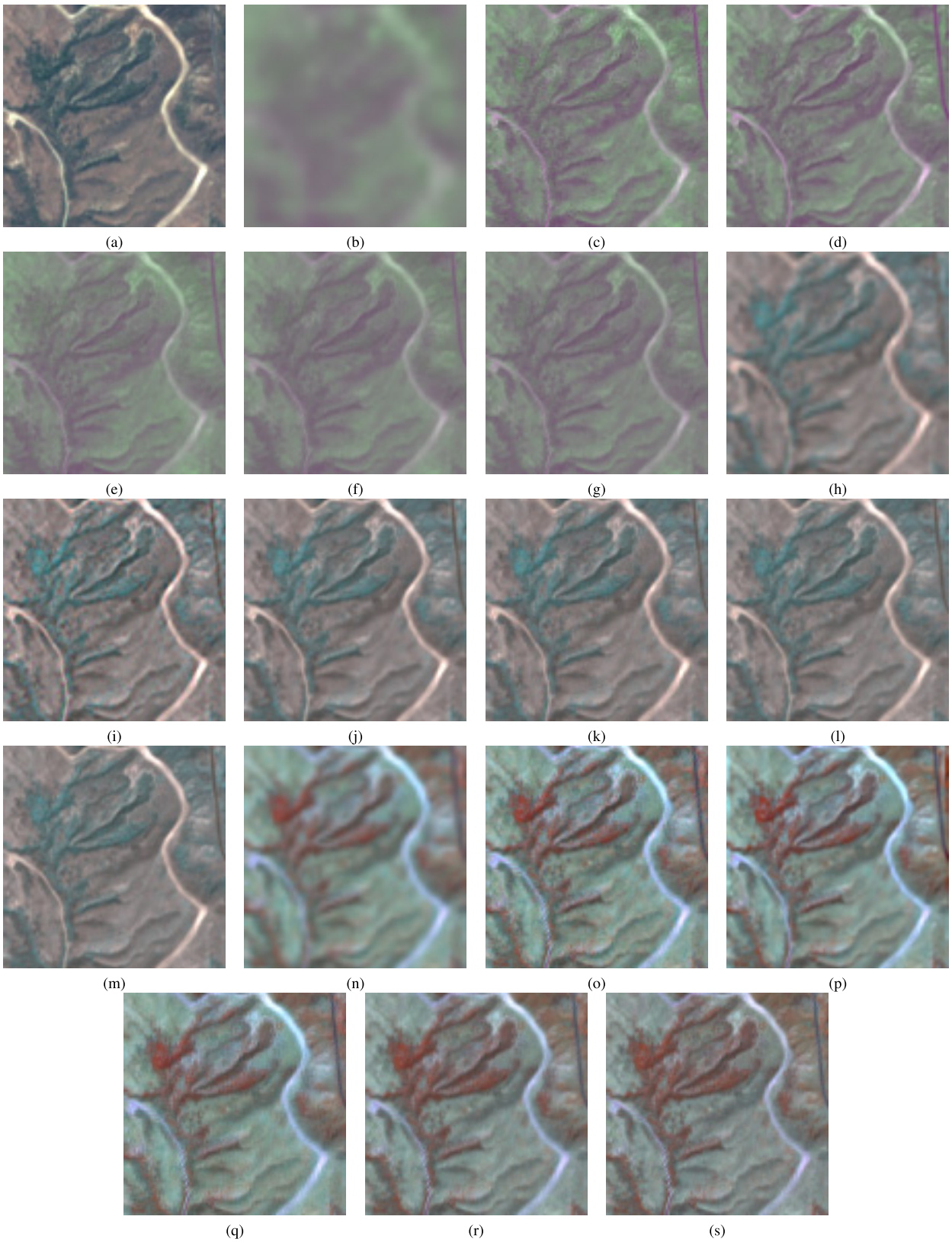


Fig. 5. Qualitative results on the real S2 images for the mountainous data set. (a) True color composite that represents the geometric detail of the scene. (b)–(g) False color composite of bands 1 and 9 (60 m). (h)–(m) False color composite of bands 5–7 (20 m). (n)–(s) False color composite of bands 8a, 11, and 12 (20 m).

Table III reports the computation times obtained using MATLAB on an Intel Core i7-7700 CPU running at 3.60 GHz, with 32 GB of RAM per image (456 × 108 pixels, representing an area of 4.92 $km^2$). The optimization problem is solved using a salsa solver, which guarantees a low computational burden. CBM3D requires on the considered image

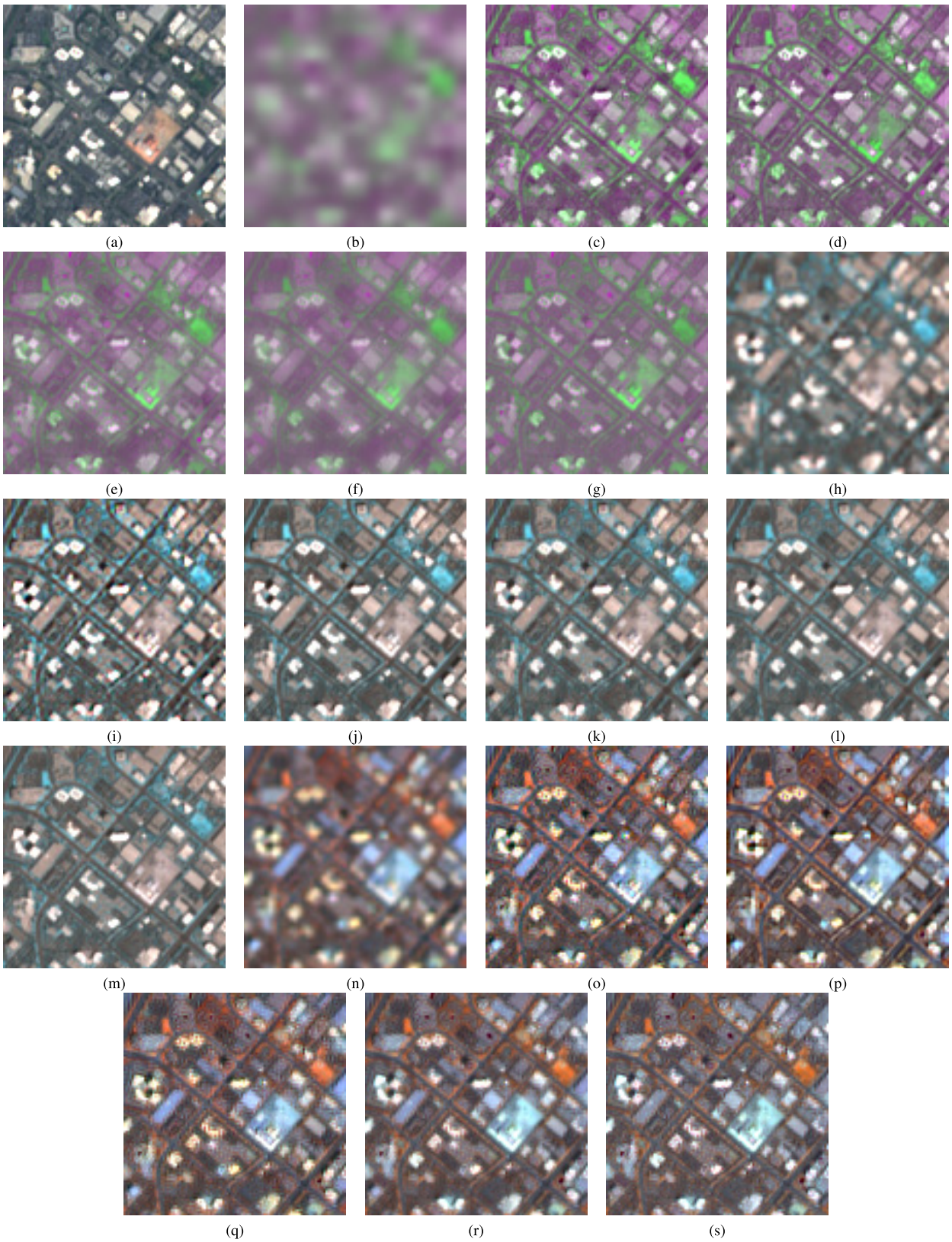


Fig. 6. Qualitative results on the real S2 images for the urban data set. (a) True color composite that represents the geometric detail of the scene. (b)–(g) False color composite of bands 1 and 9 (60 m). (h)–(m) False color composite of bands 5–7 (20 m). (n)–(s) False color composite of bands 8a, 11, and 12 (20 m).

3.5 s per iteration. In the considered implementation, we used the regularizer in the last 100 iterations, thus leading to a total time of 353.22 s per image. As expected, MuSA takes a higher computational time than noniterative methods. However, this increased time results in a significant improvement of all the other quality metrics. It is worth noting that the MuSA

TABLE III
RUNTIMES FOR SUPERRESOLVING THE EIGHT BANDS OF S2 IMAGE ($456 \times 108$ PIXELS $\approx 4.92$ Km$^2$)

| Method | Time (s) |
|---|---|
| Bicubic | 0.08 s |
| ARTPK | 24.16 s |
| MuSA | 353.22 s |
| PRACS | 0.28 s |
| HPF | 0.25 s |
| PCA | 0.31 s |

implementation can be made faster by first detecting homogeneous portions of the image for calculating the subspace and then using different parallel tasks for superresolving each portion.

## VI. CONCLUSION

In this paper, a novel method for the superresolution of MS multiresolution images has been presented. Instead of adapting a pansharpening algorithm present in the literature to the solution of the superresolution problem, the proposed approach is tailored to the specific properties of the multiresolution data both in terms of problem formulation and regularized employed. From the analysis of the experimental results, we can draw the following conclusions. Although the proposed MuSA approach requires a higher computational burden compared to noniterative methods, it outperformed the state-of-the-art methods for almost all the data sets in terms of average SRE, SAM, and UIQI. The quantitative results obtained on the simulated S2 data are confirmed by the qualitative analysis performed on the real S2 data. The MuSA was able to accurately reproduce the geometric structures present in the scene on completely different environmental scenarios: the proposed method sharpened all the low-resolution spectral channels without introducing significant distortions and artifacts.

As final remark, we would like to point out that the MuSA was able to obtain accurate results on both 60- and 20-m resolution images regardless of the initial spatial resolution, thus delivering very balanced results across the bands. This result is extremely important from the operational view point in order to fully take advantage from the spectral information provided by the MS data.

As future developments of this paper, we aim to explore the possibility of estimating the subspace in homogeneous portion of the images. This analysis can be interesting to extend the application of MuSA at large scale in order to deal with extremely heterogeneous scenes. Although the proposed method has been tested on the S 2 data, we plan to apply the proposed method to different MS multiresolution data.

## ACKNOWLEDGMENT

The authors would like to thank A. Foi for many valuable discussions, D. A. Foi, V. Katkovnik, and K. Egiazarian for kindly providing the CMB3D code, and Q. Wang, W. Shi, Z. Li, and P. M. Atkinson for providing the code of the synthetized version of the ATPRK method.

## REFERENCES

[1] G. Vivone *et al.*, "A critical comparison among pansharpening algorithms," *IEEE Trans. Geosci. Remote Sens.*, vol. 53, no. 5, pp. 2565–2586, May 2015.
[2] B. Aiazzi, L. Alparone, S. Baronti, A. Garzelli, M. Selva, and C. Chen, "25 years of pansharpening: A critical review and new developments," in *Signal and Image Processing for Remote Sensing*. Boca Raton, FL, USA: CRC Press, 2011, pp. 533–548.
[3] V. P. Shah, N. H. Younan, and R. L. King, "An efficient pan-sharpening method via a combined adaptive PCA approach and contourlets," *IEEE Trans. Geosci. Remote Sens.*, vol. 46, no. 5, pp. 1323–1335, May 2008.
[4] V. K. Shettigara, "A generalized component substitution technique for spatial enhancement of multispectral images using a higher resolution data set," *Photogram. Eng. Remote Sens.*, vol. 58, no. 5, pp. 561–567, 1992.
[5] S. Rahmani, M. Strait, D. Merkurjev, M. Moeller, and T. Wittman, "An adaptive IHS pan-sharpening method," *IEEE Geosci. Remote Sens. Lett.*, vol. 7, no. 4, pp. 746–750, Oct. 2010.
[6] Y. Zhang and G. Hong, "An IHS and wavelet integrated approach to improve pan-sharpening visual quality of natural colour IKONOS and QuickBird images," *Inf. Fusion*, vol. 6, no. 3, pp. 225–234, 2005.
[7] M. Choi, "A new intensity-hue-saturation fusion approach to image fusion with a tradeoff parameter," *IEEE Trans. Geosci. Remote Sens.*, vol. 44, no. 6, pp. 1672–1682, Jun. 2006.
[8] C. A. Laben and B. V. Brower, "Process for enhancing the spatial resolution of multispectral imagery using pan-sharpening," U.S. Patent 6 011 875, Jan. 4, 2000.
[9] B. Aiazzi, S. Baronti, and M. Selva, "Improving component substitution pansharpening through multivariate regression of MS + pan data," *IEEE Trans. Geosci. Remote Sens.*, vol. 45, no. 10, pp. 3230–3239, Oct. 2007.
[10] S. Zhong, Y. Zhang, Y. Chen, and D. Wu, "Combining component substitution and multiresolution analysis: A novel generalized BDSD pansharpening algorithm," *IEEE J. Sel. Topics Appl. Earth Observ. Remote Sens.*, vol. 10, no. 6, pp. 2867–2875, Jun. 2017.
[11] W. Wang, L. Jiao, and S. Yang, "Novel adaptive component-substitution-based pan-sharpening using particle swarm optimization," *IEEE Geosci. Remote Sens. Lett.*, vol. 12, no. 4, pp. 781–785, Apr. 2015.
[12] X. Kang, S. Li, and J. A. Benediktsson, "Pansharpening with matting model," *IEEE Trans. Geosci. Remote Sens.*, vol. 52, no. 8, pp. 5088–5099, Aug. 2014.
[13] J. L. Starck, J. Fadili, and F. Murtagh, "The undecimated wavelet decomposition and its reconstruction," *IEEE Trans. Image Process.*, vol. 16, no. 2, pp. 297–309, Feb. 2007.
[14] G. P. Nason and B. W. Silverman, "The stationary wavelet transform and some statistical applications," in *Wavelets and Statistics*, vol. 103. New York, NY, USA: Springer, 1995, pp. 281–299.
[15] A. Kallel, "MTF-adjusted pansharpening approach based on coupled multiresolution decompositions," *IEEE Trans. Geosci. Remote Sens.*, vol. 53, no. 6, pp. 3124–3145, Jun. 2015.
[16] M. N. Do and M. Vetterli, "The contourlet transform: An efficient directional multiresolution image representation," *IEEE Trans. Image Process.*, vol. 14, no. 12, pp. 2091–2106, Dec. 2005.
[17] P. J. Burt and E. H. Adelson, "The Laplacian pyramid as a compact image code," *IEEE Trans. Commun.*, vol. 31, no. 4, pp. 532–540, Apr. 1983.
[18] B. Aiazzi, L. Alparone, S. Baronti, A. Garzelli, and M. Selva, "MTF-tailored multiscale fusion of high-resolution MS and PAN imagery," *Photogramm. Eng. Remote Sens.*, vol. 72, no. 5, pp. 591–596, May 2006.
[19] P. Chavez, Jr., S. C. Sides, and J. A. Anderson, "Comparison of three different methods to merge multiresolution and multispectral data: Landsat TM and SPOT panchromatic," *Photogramm. Eng. Remote Sens.*, vol. COM-57, no. 3, pp. 295–303, 1991.
[20] Y. Zeng, W. Huang, M. Liu, H. Zhang, and B. Zou, "Fusion of satellite images in urban area: Assessing the quality of resulting images," in *Proc. IEEE 18th Int. Conf. Geoinf.*, Jun. 2010, pp. 1–4.
[21] M. V. Joshi, L. Bruzzone, and S. Chaudhuri, "A model-based approach to multiresolution fusion in remotely sensed images," *IEEE Trans. Geosci. Remote Sens.*, vol. 44, no. 9, pp. 2549–2562, Sep. 2006.
[22] X. He, L. Condat, J. M. Bioucas-Dias, J. Chanussot, and J. Xia, "A new pansharpening method based on spatial and spectral sparsity priors," *IEEE Trans. Image Process.*, vol. 23, no. 9, pp. 4160–4174, Sep. 2014.

[23] F. Palsson, J. R. Sveinsson, and M. O. Ulfarsson, "A new pansharpening algorithm based on total variation," *IEEE Geosci. Remote Sens. Lett.*, vol. 11, no. 1, pp. 318–322, Jan. 2014.
[24] B. Aiazzi, L. Alparone, S. Baronti, L. Santurri, and M. Selva, "Spatial resolution enhancement of ASTER thermal bands," *Proc. SPIE*, vol. 5982, p. 59821G, Oct. 2005.
[25] D. Fasbender, D. Tuia, P. Bogaert, and M. Kanevski, "Support-based implementation of Bayesian data fusion for spatial enhancement: Applications to ASTER thermal images," *IEEE Geosci. Remote Sens. Lett.*, vol. 5, no. 4, pp. 598–602, Oct. 2008.
[26] P. Sirguey, R. Mathieu, Y. Arnaud, M. M. Khan, and J. Chanussot, "Improving MODIS spatial resolution for snow mapping using wavelet fusion and ARSIS concept," *IEEE Geosci. Remote Sens. Lett.*, vol. 5, no. 1, pp. 78–82, Jan. 2008.
[27] A. P. Trishchenko, Y. Luo, and K. V. Khlopenkov, "A method for downscaling MODIS land channels to 250-m spatial resolution using adaptive regression and normalization," *Proc. SPIE*, vol. 6366, p. 636607, Oct. 2006.
[28] Q. Wang, "Downscaling MODIS images with area-to-point regression Kriging," *Remote Sens. Environ.*, vol. 166, pp. 191–204, Sep. 2015.
[29] M. H. Ribeiro Sales, C. M. Souza, and P. C. Kyriakidis, "Fusion of MODIS images using Kriging with external drift," *IEEE Trans. Geosci. Remote Sens.*, vol. 51, no. 4, pp. 2250–2259, Apr. 2013.
[30] H. Tonooka, "Resolution enhancement of ASTER shortwave and thermal infrared bands based on spectral similarity," *Proc. SPIE*, vol. 5657, pp. 9–20, Jan. 2005.
[31] Q. M. Wang, W. Z. Shi, Z. B. Li, and P. M. Atkinson, "Fusion of sentinel-2 images," *Remote Sens. Environ.*, vol. 187, pp. 241–252, Dec. 2016.
[32] A. D. Vaiopoulos and K. Karantzalos, "Pansharpening on the narrow VNIR and SWIR spectral bands of sentinel-2," *Int. Arch. Photogramm., Remote Sens. Spatial Inf. Sci.*, vol. XLI-B7, pp. 723–730, Jun. 2016.
[33] M. Selva, B. Aiazzi, F. Butera, L. Chiarantini, and S. Baronti, "Hyper-sharpening: A first approach on SIM-GA data," *IEEE J. Sel. Topics Appl. Earth Observ. Remote Sens.*, vol. 8, no. 6, pp. 3008–3024, Jun. 2015.
[34] C. Lanaras, J. Bioucas-Dias, E. Baltsavias, and K. Schindler, "Super-resolution of multispectral multiresolution images from a single sensor," in *Proc. IEEE Conf. Comput. Vis. Pattern Recognit. Workshops (CVPRW)*, Jul. 2017, pp. 1505–1513.
[35] N. Brodu, "Super-resolving multiresolution images with band-independent geometry of multispectral pixels," *IEEE Trans. Geosci. Remote Sens.*, vol. 55, no. 8, pp. 4610–4617, Aug. 2017.
[36] A. Danielyan, V. Katkovnik, and K. Egiazarian, "BM3D frames and variational image deblurring," *IEEE Trans. Image Process.*, vol. 21, no. 4, pp. 1715–1728, Apr. 2012.
[37] J. Zhang, D. Zhao, and W. Gao, "Group-based sparse representation for image restoration," *IEEE Trans. Image Process.*, vol. 23, no. 8, pp. 3336–3351, Aug. 2014.
[38] K. Dabov, A. Foi, V. Katkovnik, and K. Egiazarian, "Color image denoising via sparse 3D collaborative filtering with grouping constraint in luminance-chrominance space," in *Proc. IEEE Int. Conf. Image Process. (ICIP)*, vol. 1, Sep./Oct. 2007, pp. I-313–I-316.
[39] K. Egiazarian and V. Katkovnik, "Single image super-resolution via BM3D sparse coding," in *Proc. IEEE 23rd Eur. Signal Process. Conf. (EUSIPCO)*, Aug./Sep. 2015, pp. 2849–2853.
[40] M. V. Afonso, J.-M. Bioucas-Dias, and M. A. T. Figueiredo, "Fast image recovery using variable splitting and constrained optimization," *IEEE Trans. Image Process.*, vol. 19, no. 9, pp. 2345–2356, Sep. 2010.
[41] M. V. Afonso, J. M. Bioucas-Dias, and M. A. T. Figueiredo, "An augmented Lagrangian approach to the constrained optimization formulation of imaging inverse problems," *IEEE Trans. Image Process.*, vol. 20, no. 3, pp. 681–695, Mar. 2011.
[42] M. Simoes, J. Bioucas-Dias, L. B. Almeida, and J. Chanussot, "A convex formulation for hyperspectral image superresolution via subspace-based regularization," *IEEE Trans. Geosci. Remote Sens.*, vol. 53, no. 6, pp. 3373–3388, Jun. 2015.
[43] Q. Wei, J. Bioucas-Dias, N. Dobigeon, J.-Y. Tourneret, M. Chen, and S. Godsill, "Multiband image fusion based on spectral unmixing," *IEEE Trans. Geosci. Remote Sens.*, vol. 54, no. 12, pp. 7236–7249, Dec. 2016.
[44] P. L. Combettes and V. R. Wajs, "Signal recovery by proximal forward-backward splitting," *Multiscale Model. Simul.*, vol. 4, no. 4, pp. 1168–1200, 2005.
[45] S. V. Venkatakrishnan, C. A. Bouman, and B. Wohlberg, "Plug-and-play priors for model based reconstruction," in *Proc. IEEE Global Conf. Signal Inf. Process.*, Dec. 2013, pp. 945–948.
[46] J.-J. Moreau, "Proximité et dualité dans un espace hilbertien," *Bull. Soc. Math. France*, vol. 93, no. 2, pp. 273–299, 1965.
[47] A. M. Teodoro, J. M. Bioucas-Dias, and M. A. T. Figueiredo. (Jan. 2018). "Scene-adapted plug-and-play algorithm with guaranteed convergence: Applications to data fusion in imaging." [Online]. Available: https://arxiv.org/abs/1801.00605
[48] U. Müller-Wilm, J. Louis, R. Richter, F. Gascon, and M. Niezette, "Sentinel-2 level 2A prototype processor: Architecture, algorithms and first results," in *Proc. ESA Living Planet Symp.*, Edinburgh, U.K., 2013, pp. 9–13.
[49] G. Vane, R. O. Green, T. G. Chrien, H. T. Enmark, E. G. Hansen, and W. M. Porter, "The airborne visible/infrared imaging spectrometer (AVIRIS)," *Remote Sens. Environ.*, vol. 44, nos. 2–3, pp. 127–143, 1993.
[50] "Sentinel-2 data quality report," Eur. Space Agency, Paris, France, Tech. Rep. S2-PDGS-MPC-DQR, Jul. 2016, p. 20, no. 5.
[51] S. Boyd, N. Parikh, E. Chu, B. Peleato, and J. Eckstein, "Distributed optimization and statistical learning via the alternating direction method of multipliers," *Found. Trends Mach. Learn.*, vol. 3, no. 1, pp. 1–122, Jan. 2011.
[52] R. H. Yuhas, A. F. Goetz, and J. W. Boardman, "Discrimination among semi-arid landscape endmembers using the Spectral Angle Mapper (SAM) algorithm," in *Proc. Summaries 3rd Annu. JPL Airborne Geosci. Workshop*, vol. 1, 1992, pp. 147–149.
[53] Z. Wang and A. C. Bovik, "A universal image quality index," *IEEE Signal Process. Lett.*, vol. 9, no. 3, pp. 81–84, Mar. 2002.
[54] J. Choi, K. Yu, and Y. Kim, "A new adaptive component-substitution-based satellite image fusion by using partial replacement," *IEEE Trans. Geosci. Remote Sens.*, vol. 49, no. 1, pp. 295–309, Jan. 2011.

**Claudia Paris** (M'16) received the Laurea (B.S.) degree in telecommunication engineering, the Laurea Specialistica (M.S.) *(summa cum laude)* degree in telecommunication engineering, and the Ph.D. degree in information and communication technology from the University of Trento, Trento, Italy, in 2010, 2012, and 2016, respectively. She accomplished the Honors Master Program in Research within the master's degree in telecommunication engineering in 2012.

Since 2014, she has been a Teaching Assistant with the Department of Information Engineering and Computer Science, University of Trento. She is currently involved in the analysis of multitemporal images acquired by the European Space Agency (ESA) Sentinel-2 satellite constellation for the automatic update of land cover maps in the context of the Scientific Exploitation of Operational Missions Sentinel-2 for Science ESA Program. Her research interests include image processing and machine learning with applications to remote sensing image analysis, remote sensing single-date and time-series image classification, land cover map update, and fusion of multisource remote sensing data for the estimation of biophysical parameters. She conducts research on these topics within the frameworks of national and international projects.

Dr. Paris received the very prestigious Symposium Prize Paper Award at the 2016 IEEE International Symposium on Geoscience and Remote Sensing, Beijing, China, and the 2017 IEEE International Symposium on Geoscience and Remote Sensing, Fort Worth, TX, USA. She is a Reviewer for many international journals, including the IEEE TRANSACTIONS ON GEOSCIENCE AND REMOTE SENSING, the IEEE JOURNAL OF SELECTED TOPICS IN APPLIED EARTH OBSERVATIONS AND REMOTE SENSING, and the IEEE GEOSCIENCE AND REMOTE SENSING LETTERS.

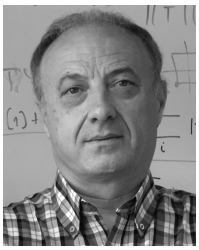

**José Bioucas-Dias** (S'87–M'95–SM'15–F'17) received the Electrical Engineering, M.Sc., Ph.D., and Habilitation degrees in electrical and computer engineering from the Instituto Superior Técnico (IST), Universidade Técnica de Lisboa, Lisbon, Portugal, in 1985, 1991, 1995, and 2007, respectively.

Since 1995, he has been with the Department of Electrical and Computer Engineering, IST, Universidade de Lisboa, where he is currently a Professor and teaches inverse problems in imaging and electric communications. He is also a Senior Researcher with the Pattern and Image Analysis Group, Instituto de Telecomunicações, which is a private nonprofit research institution. His research interests include inverse problems, signal and image processing, pattern recognition, optimization, and remote sensing. He has introduced scientific contributions in the areas of imaging inverse problems, statistical image processing, optimization, phase estimation, and phase unwrapping and in various imaging applications, such as hyperspectral and radar imaging.

Dr. Bioucas-Dias received the IEEE GRSS David Landgrebe Award in 2017. He was included in Thomson Reuters' Highly Cited Researchers 2015 list.

**Lorenzo Bruzzone** (S'95–M'98–SM'03–F'10) received the Laurea (M.S.) degree *(summa cum laude)* in electronic engineering and the Ph.D. degree in telecommunications from the University of Genoa, Genoa, Italy, in 1993 and 1998, respectively.

He is currently a Full Professor of telecommunications with the University of Trento, Trento, Italy, where he teaches remote sensing, radar, and digital communications. He is also the Founder and the Director of the Remote Sensing Laboratory, Department of Information Engineering and Computer Science, University of Trento. He is a principal investigator of many research projects. Among others, he is also a Principal Investigator of the Radar for Icy Moon Exploration instrument in the framework of the JUpiter ICy moons Explorer Mission of the European Space Agency. He has authored or co-authored 218 scientific publications in referred international journals (157 in IEEE journals), over 290 papers in conference proceedings, and 21 book chapters. He has edited/co-edited 18 books/conference proceedings and one scientific book. His research interests include the areas of remote sensing, radar and synthetic aperture radar, signal processing, machine learning, and pattern recognition. He promotes and supervises research on these topics within the frameworks of many national and international projects.

Dr. Bruzzone has been a member of the Administrative Committee of the IEEE Geoscience and Remote Sensing Society (GRSS) since 2009. He is currently a member of the Permanent Steering Committee of the IEEE International Workshop on the Analysis of Multi-Temporal Remote-Sensing Images series. He received the First Place in the Student Prize Paper Competition at the 1998 IEEE International Geoscience and Remote Sensing Symposium (IGARSS), Seattle. He was a recipient of many international and national honors and awards, including the IEEE GRSS 2015 Outstanding Service Award and the 2017 IEEE IGARSS Symposium Prize Paper Award. Since 2003, he has been the Chair of the Society of Photographic Instrumentation Engineers Conference on Image and Signal Processing for Remote Sensing. He has been the Founder of the *IEEE Geoscience and Remote Sensing Magazine*. He was a guest co-editor of many special issues of international journals. He is the Co-Founder of the IEEE International Workshop on the Analysis of Multi-Temporal Remote-Sensing Images series. He was the Editor-in-Chief of the *IEEE Geoscience and Remote Sensing Magazine* from 2013 to 2017. He is an Associate Editor of the IEEE TRANSACTIONS ON GEOSCIENCE AND REMOTE SENSING. He was invited as a keynote speaker in more than 30 international conferences and workshops. He was a Distinguished Speaker of the IEEE Geoscience and Remote Sensing Society from 2012 to 2016. His papers are highly cited, as proven by the total number of citations (over 24 500) and the value of the h-index (72) (source: Google Scholar).